

A gradient flow model for ground state calculations in Wigner formalism based on density functional theory

Guanghui Hu¹, Ruo Li^{2,3}, and Hongfei Zhan^{*4}

¹State Key Laboratory of Internet of Things for Smart City and Department of Mathematics, University of Macau, Macao SAR, 999078, People's Republic of China

²CAPT, LMAM and School of Mathematical Sciences, Peking University, Beijing, 100871, People's Republic of China

³Chongqing Research Institute of Big Data, Peking University, Chongqing, 401121, People's Republic of China

⁴School of Mathematical Sciences, Peking University, Beijing, 100871, People's Republic of China

Abstract

In this paper, a gradient flow model is proposed for conducting ground state calculations in Wigner formalism of many-body system in the framework of density functional theory. More specifically, an energy functional for the ground state in Wigner formalism is proposed to provide a new perspective for ground state calculations of the Wigner function. Employing density functional theory, a gradient flow model is designed based on the energy functional to obtain the ground state Wigner function representing the whole many-body system. Subsequently, an efficient algorithm is developed using the operator splitting method and the Fourier spectral collocation method, whose numerical complexity of single iteration is $O(n_{\text{DoF}} \log n_{\text{DoF}})$. Numerical experiments demonstrate the anticipated accuracy, encompassing the one-dimensional system with up to 2^{21} particles and the three-dimensional system with defect, showcasing the potential of our approach to large-scale simulations and computations of systems with defect.

Keyword: Wigner function; ground state; density functional theory; gradient flow model

1 Introduction

In the Schrödinger formalism, density functional theory [39] (DFT) is one of the most widely used approximate model in electronic structure calculations [30, 31, 24]. Theoretically, it has been proved that three dimensional ground state electron density is a fundamental quantity in a given many-body system [18]. Numerically, the ground state density is often determined by either energy minimization or solving the self-consistent Kohn-Sham equations. Despite the diversity of numerical methods for solving the ground state in Schrödinger formalism, significant challenges arise in large-scale simulations, encompassing algorithm scalability [26, 27, 11], convergence issue [53] and even the memory requirement for depicting the whole system. It is worth mentioning that Das et al achieved ab-initio simulations of quasicrystals and interacting extended defects in metallic alloys consisting of hundreds of thousands electrons in [10]. However, the sheer number of orbitals that need to be solved remains a fundamental problem for large-scale simulations. The Wigner formalism offers an alternative approach to both theoretically describe and numerically solve quantum systems, holding the potential for efficiency simulations of large-scale systems.

*Corresponding Author

In contrast to the conventional Schrödinger wave function in Hilbert space, the Wigner phase-space quasi-distribution function [47] provides an equivalent approach to describe quantum object that bears a close analogy to classical mechanics [51]. The Wigner formalism has been applied to a variety of situations ranging from atomic physics [44] to quantum electronic transport [32, 46] and many-body quantum systems [37, 48]. Furthermore, both pure and mixed states of a quantum system can be handled in a unified manner by Wigner function [6]. Hence, in the context of density functional theory, a set of Kohn-Sham orbitals can be depicted by a single mixed state Wigner function, which sums up all the pure state Wigner functions corresponding to each orbital. This facilitates the ground state calculations based on a single Wigner function instead of multiple wave functions for Kohn-Sham orbitals. All these features motivate the research on developing models and numerical methods to determine the Wigner functions of a quantum system.

Different from the situation for Schrödinger equation that there have been a number of mature approximate models and numerical methods, more efforts are required towards the Wigner functions. The first attempts to simulate quantum phenomena by the Wigner function were [13, 14] for one-dimensional one-body systems. Subsequently, Wigner simulations were accomplished using the spectral collocation method combined with the operator splitting method [1, 2]. Recently, several methods were designed for the simulation based on Wigner function, including the spectral element method [40, 48, 7, 49], the spectral decomposition [45], the moment method [5, 23, 52], the discontinuous Galerkin method [16], the Gaussian beam method [50], the weighted essentially non-oscillatory scheme [12], and the exponential integrator [15]. Additionally, various stochastic methods have been developed, such as the signed particle Wigner Monte Carlo method [28, 29, 38] and path integral method [22, 21, 4]. In many-body scenarios, the Wigner based simulations have been achieved by the advective-spectral-mixed method [48], the Monte Carlo method [33, 35, 36] and the method based on branching random walk [41]. For dynamic studies of a given system, an initial state should be specified, which is typically the ground state. Numerous theoretical works have derived ground state Wigner functions for specific models, such as the hydrogen atom [9], the closed-shell atom [42], and the Moshinsky atom [8]. In terms of numerical computations, Sellier and Dimov proposed a viable framework in [34] for addressing both time-dependent and time-independent problems of three-dimensional systems using the Monte Carlo method. On the contrary, deterministic methods are limited to one-dimensional systems, encompassing the modified tau spectral method [19, 20] and the Fourier transform [3]. In our previous work [52], ground state calculations in Wigner formalism for DFT examples were accomplished using simplified Grad moment method combined with an imaginary time propagation method. However, deterministic approaches for ground state calculations in Wigner formalism with density functional theory remain limited to two-body systems.

In this paper, in the category of deterministic approach, a gradient flow model is proposed for ground state calculations in Wigner formalism of many-body systems within the framework of density functional theory. In particular, a gradient flow model for one-body systems is firstly derived. Introducing density functional theory, this model is extended to many-body systems by solving a single mixed state Wigner function. To enhance computational efficiency, an operator splitting scheme is adopted to decompose the original system into three sub-equations, enabling parallel implementation. Based on the structure of derived equations, the Fourier pseudo-spectral method is employed for discretization in both \mathbf{x} and \mathbf{p} directions. Consequently, each sub-equation can be solved with $O(n_{\text{DoF}})$ computational cost for degree of freedom (DoF) number n_{DoF} , resulting in an overall computational cost of single time iteration as $O(n_{\text{DoF}} \log n_{\text{DoF}})$. To validate the proposed method, two toy models are presented, which are generated by the periodic extension of two-body systems. The first example is a one-dimensional delta-interacting system with a local density approximation, where the ground state for the system with up to 2^{21} electrons are calculated. The second example is a three-dimensional system with Coulomb interaction, including a scenarios with a defect. Anticipated spectral accuracy can be successfully observed in all the computations. And these examples demonstrate the potential applications of our approach to large-scale systems and systems with defects.

Our contributions of this work can be summarized as follows.

1. The energy functional for the ground state in Wigner formalism is proposed, providing a new perspective for ground state calculations in Wigner formalism.

2. A gradient flow model is presented for ground state calculations in Wigner formalism of many-body systems with the aid of density functional theory. To our best knowledge, our method is the first deterministic approach solving three-dimensional many-body ground states in Wigner formalism.
3. Efficient algorithm is developed for the model, whose computational cost of single iteration is $O(n_{\text{DoF}} \log n_{\text{DoF}})$ for DoF number n_{DoF} .
4. Numerical simulations successfully deliver the desired results for the one-dimensional system with up to 2^{21} particles and the three-dimensional system with defect, fully demonstrating the descriptive capability of the Wigner formalism, and showcasing the potential of our approach to large-scale simulations and computations of systems with defect.

The rest of this paper is organized as follows: In Sect. 2, the eigenvalue problem in Wigner formalism is briefly introduced, based on which a gradient flow model for one-body systems is derived. Incorporating density functional theory, the gradient model is extended to many-body systems in Sect. 3. Sect. 4 discussion the implementation of an operator splitting method and the Fourier pseudospectral method for efficient simulations of the model. Numerical results are demonstrated in Sect. 5. Finally, a conclusion of this paper and the discussion of future work are provided in Sect. 6.

For simplicity, the Hartree atomic unit is adopted hereafter, i.e., take $\hbar = m = e = 1$ for reduced plank constant, electron mass and electron charge.

2 A gradient flow model for Wigner formalism

In this section, the Wigner formalism and the Wigner eigenvalue problem are first introduced. Subsequently, a gradient flow model based on the Weyl transform of the energy operator is derived.

2.1 Wigner formalism

Given the time-independent Schrödinger equation,

$$\left(-\frac{\nabla^2}{2} + V(\mathbf{x})\right)\psi_j(\mathbf{x}) = E_j\psi_j(\mathbf{x}), \quad j = 0, 1, 2, \dots, \quad (1)$$

where ψ_j is the j -th eigenfunction with eigenvalue E_j and forms an orthonormal set whose eigenvalues are in increasing order. We have the density matrix,

$$\rho(\mathbf{x}, \mathbf{x}') = \sum_{j=0}^{\infty} P_j \psi_j(\mathbf{x}) \psi_j^*(\mathbf{x}'), \quad (2)$$

here P_j is the probability of obtaining the j -th eigenstate. The Wigner function $f(\mathbf{x}, \mathbf{p}) \in \mathbb{R}^{2D}$ is defined by applying the Weyl transform to the density matrix,

$$f(\mathbf{x}, \mathbf{p}) := \frac{1}{(2\pi)^D} \int_{\mathbb{R}^D} \rho\left(\mathbf{x} + \frac{\mathbf{y}}{2}, \mathbf{x} - \frac{\mathbf{y}}{2}\right) \exp(-i\mathbf{p} \cdot \mathbf{y}) d\mathbf{y}, \quad (3)$$

where D is the dimensionality of the system, $i = \sqrt{-1}$ represents the imaginary unit. Following the basic property of the Weyl transform, we have the expression of the density and energy as follows,

$$\rho(\mathbf{x}) = \int_{\mathbb{R}^D} f(\mathbf{x}, \mathbf{p}) d\mathbf{p}, \quad (4)$$

$$E = \iint_{\mathbb{R}^D \times \mathbb{R}^D} \left(\frac{|\mathbf{p}|^2}{2} + V\right) f(\mathbf{x}, \mathbf{p}) d\mathbf{x} d\mathbf{p}, \quad (5)$$

where V is the prescribed potential function. Then we have the normalization condition for the Wigner function

$$\iint_{\mathbb{R}^D \times \mathbb{R}^D} f(\mathbf{x}, \mathbf{p}) d\mathbf{x} d\mathbf{p} = 1. \quad (6)$$

Based on the time-independent Schrödinger equation, one can derive the following eigenvalue problem [17, 52],

$$H_w f(\mathbf{x}, \mathbf{p}) := \frac{1}{2} \left(-\frac{\nabla_{\mathbf{x}}^2}{4} f(\mathbf{x}, \mathbf{p}) + |\mathbf{p}|^2 f(\mathbf{x}, \mathbf{p}) + \int_{\mathbb{R}^D} V_{\text{eig}}(\mathbf{x}, \mathbf{p}') f(\mathbf{x}, \mathbf{p}' - \mathbf{p}') d\mathbf{p}' \right) = E f(\mathbf{x}, \mathbf{p}), \quad (7)$$

where

$$V_{\text{eig}}(\mathbf{x}, \mathbf{p}) = \frac{1}{(2\pi)^D} \int_{\mathbb{R}^D} S_V(\mathbf{x}, \mathbf{y}) \exp(-i\mathbf{p} \cdot \mathbf{y}) d\mathbf{y}, \quad (8)$$

$$S_V(\mathbf{x}, \mathbf{y}) = V\left(\mathbf{x} + \frac{\mathbf{y}}{2}\right) + V\left(\mathbf{x} - \frac{\mathbf{y}}{2}\right). \quad (9)$$

Although the ground state in Wigner formalism can be obtained by directly solving (7), the problem dimensionality actually doubles. This issue becomes even more severe when addressing the ground state of many-body systems. Therefore, it is preferable to determine the many-body ground state through energy optimization, which focuses the computation on only single Wigner function, leveraging the descriptive capability of the Wigner formalism. In the next subsection, the energy functional for one-body systems in Wigner formalism is proposed, which is a crucial component for developing the Wigner gradient flow model for many-body systems.

2.2 Energy functional for one-body systems in Wigner formalism

It is noted that the basic property of the Weyl transform implies that

$$\iint_{\mathbb{R}^D \times \mathbb{R}^D} |f(\mathbf{x}, \mathbf{p})|^2 d\mathbf{x} d\mathbf{p} = \iint_{\mathbb{R}^D \times \mathbb{R}^D} f(\mathbf{x}, \mathbf{p})^2 d\mathbf{x} d\mathbf{p} = (2\pi)^{-D}. \quad (10)$$

Since H_w in Eq. (7) is Hermitian, we can intuitively define the energy functional as

$$E_{\text{one}}[f] := (2\pi)^D \iint_{\mathbb{R}^D \times \mathbb{R}^D} f(\mathbf{x}, \mathbf{p})^* H_w f(\mathbf{x}, \mathbf{p}). \quad (11)$$

Owing to the variational principle, the ground state Wigner function can be obtained by minimizing $E_{\text{one}}[f]$ in (11). To demonstrate the validity of this process, we have the following theorem.

Theorem 2.1. *For one-body system, suppose the validity of the change of variables $\mathbf{u} = \mathbf{x} + \mathbf{y}/2$, $\mathbf{v} = \mathbf{x} - \mathbf{y}/2$, the ground state Wigner function and the corresponding energy can be obtained by minimizing $E_{\text{one}}[f]$ over real-valued functions in $L_2(\mathbb{R}^{2D})$ with the constraint in Eq. (6).*

Proof. Let $g : \mathbb{R}^{2D} \rightarrow \mathbb{R}$, $g \in L_2(\mathbb{R}^{2D})$, it follows the hypothesis that there exists expansion

$$g(\mathbf{x}, \mathbf{p}) = \sum_{j,k=0}^{\infty} c_{jk} f_{jk}(\mathbf{x}, \mathbf{p}), \quad (12)$$

$$f_{jk}(\mathbf{x}, \mathbf{p}) = \frac{1}{(2\pi)^D} \int_{\mathbb{R}^D} \psi_k^*(\mathbf{x} - \frac{\mathbf{y}}{2}) \psi_j(\mathbf{x} + \frac{\mathbf{y}}{2}) \exp(-i\mathbf{p} \cdot \mathbf{y}) d\mathbf{y}, \quad (13)$$

$$c_{jk} = (g, f_{jk}) / (f_{jk}, f_{jk}), \quad (14)$$

where (\cdot, \cdot) is the inner produce in $L_2(\mathbb{R}^{2D})$.

Particularly, f_{jj} recovers the Wigner function corresponds to the j -th eigenstate, and

$$(f_{jk}, f_{j'k'}) = (2\pi)^{-D} \delta_{jj'} \delta_{kk'}, \quad (15)$$

$$H_w f_{jk} = \frac{E_j + E_k}{2} f_{jk}, \quad (16)$$

$$\iint_{\mathbb{R}^D \times \mathbb{R}^D} f_{jk} d\mathbf{x} d\mathbf{p} = \delta_{jk}, \quad (17)$$

$$\iint_{\mathbb{R}^D \times \mathbb{R}^D} \left(\frac{|\mathbf{p}|^2}{2} + V(\mathbf{x}) \right) f_{jj} d\mathbf{x} d\mathbf{p} = E_j, \quad (18)$$

where δ_{jk} is the Kronecker delta symbol.

One can deduce from the normalization condition Eq. (6) that

$$\sum_{j=0}^{\infty} |c_{jj}|^2 = 1. \quad (19)$$

Finally, by substitution of Eq. (12) into Eq. (11) we find

$$E_{\text{one}}[g] = \sum_{j,k=0}^{\infty} \frac{E_j + E_k}{2} |c_{jk}|^2 = \sum_{j=0}^{\infty} E_j |c_{jj}|^2 + \sum_{0 \leq j < k} \frac{E_j + E_k}{2} (|c_{jk}|^2 + |c_{kj}|^2) \geq E_0, \quad (20)$$

with the equality holds if and only if $c_{jk} = 1$ when $j = k = 0$, and $c_{jk} = 0$ otherwise. Moreover, it follows Eq. (18) that $E_{\text{one}}[f_{00}] = E_0$ in this situation. \square

Based on the above theorem, two approaches can be considered for the ground state calculations in Wigner formalism, i.e., optimization approach for minimizing the energy functional, and solving the equation derived from the first-order necessary condition. In our previous work [52], the latter approach has been explored, in which the ground state of a one-dimensional two-body system is computed. However, extending this method to three-dimensional cases is a nontrivial task. Moreover, applying the method to more complicated system requires calculating more Wigner functions corresponding to different orbitals, greatly increasing computational demands. In the next section, a gradient flow model for ground state calculations in Wigner formalism of many-body systems is presented, fully utilizing the depicting capability of the Wigner formalism and reducing the computational burden associated with simulating numerous Wigner functions.

3 A Wigner gradient flow model for the Kohn-Sham model

Utilizing the result in Section 2.2, one can derive the Wigner gradient flow model for one-body systems over real-valued functions in $L_2(\mathbb{R}^D \times \mathbb{R}^D)$ as

$$\begin{cases} \frac{\partial}{\partial t} f(\mathbf{x}, \mathbf{p}, t) = -\frac{\delta E_{\text{one}}[f]}{\delta f(\mathbf{x}, \mathbf{p}, t)} = -2(2\pi)^D H_w f(\mathbf{x}, \mathbf{p}, t), & t > 0, \\ \iint_{\mathbb{R}^D \times \mathbb{R}^D} f(\mathbf{x}, \mathbf{p}, t) d\mathbf{x} d\mathbf{p} = 1, & t \geq 0. \end{cases} \quad (21)$$

In this section, the Kohn-Sham model is introduced to resolve the high dimensionality of many-body problems. Following a similar process as the last section, the energy functional of many-body systems in Wigner formalism is presented, based on which a Wigner gradient flow model will be developed.

3.1 The Kohn-Sham model

Within the context of density functional theory, the many-body wave function can be approximated by the Slater determinant of the Kohn-Sham orbital functions, which satisfy the following Kohn-Sham equations,

$$\left(-\frac{\nabla^2}{2} + V_{\text{KS}}[\rho](\mathbf{x}) \right) \psi_j^{\text{KS}}(\mathbf{x}) = \varepsilon_j \psi_j^{\text{KS}}(\mathbf{x}), \quad j = 1, 2, \dots, \quad (22)$$

where

$$\rho(\mathbf{x}) = \sum_{j=1}^{N_o} P_j^{\text{KS}} \rho_j^{\text{KS}}(\mathbf{x}), \quad \rho_j^{\text{KS}}(\mathbf{x}) = |\psi_j^{\text{KS}}(\mathbf{x})|^2, \quad (23)$$

N_o is the number of occupied orbitals, ψ_j^{KS} are the j -th eigenstate with eigenvalue ε_j in increasing order, and P_j^{KS} is the occupation number of ψ_j^{KS} . In particular,

$$V_{\text{KS}}[\rho](\mathbf{x}) = V_{\text{ext}}(\mathbf{x}) + U_{\text{H}}[\rho](\mathbf{x}) + V_{\text{xc}}[\rho](\mathbf{x}). \quad (24)$$

Here V_{ext} stands for the external potential. The second term depicts the electron-electron interaction subject to the interaction function V_{ee} , which can be attained following the variational principle of the interaction energy,

$$U_{\text{H}}[\rho] = \frac{1}{2} \iint_{\mathbb{R}^D \times \mathbb{R}^D} V_{\text{ee}}(|\mathbf{x} - \mathbf{x}'|) \rho(\mathbf{x}) \rho(\mathbf{x}') d\mathbf{x} d\mathbf{x}', \quad (25)$$

as

$$V_{\text{H}}[\rho](\mathbf{x}) = \frac{\delta U_{\text{H}}[\rho]}{\delta \rho(\mathbf{x})} = \int_{\mathbb{R}^D} V_{\text{ee}}(|\mathbf{x} - \mathbf{x}'|) \rho(\mathbf{x}') d\mathbf{x}'. \quad (26)$$

And the last term

$$V_{\text{xc}}[\rho](\mathbf{x}) = \frac{\delta E_{\text{xc}}[\rho]}{\rho(\mathbf{x})} \quad (27)$$

is the exchange-correlation potential. Since an analytic expression of V_{xc} is often unknown in the most situations, approximations are required for the this term.

Subsequently, the descriptive capability of the Wigner formalism can be presented in a straightforward way in the sense that single mixed state Wigner function represents the whole DFT system,

$$f_{\text{gs}}^{\text{KS}}(\mathbf{x}, \mathbf{p}) = \frac{1}{(2\pi)^D} \int_{\mathbb{R}^D} \rho_{\text{gs}}^{\text{KS}} \left(\mathbf{x} + \frac{\mathbf{y}}{2}, \mathbf{x} - \frac{\mathbf{y}}{2} \right) \exp(-i\mathbf{p} \cdot \mathbf{y}) d\mathbf{y}, \quad (28)$$

where

$$\rho_{\text{gs}}^{\text{KS}}(\mathbf{x}, \mathbf{x}') = \sum_{j=1}^{N_o} P_j^{\text{KS}} \psi_j^{\text{KS}}(\mathbf{x}) (\psi_j^{\text{KS}})^*(\mathbf{x}'). \quad (29)$$

For brevity, we focus on the closed-shell system in the following, i.e., taking $P_j^{\text{KS}} = P_{\text{occ}}^{\text{cs}} = 2$ for all $1 \leq j \leq N_o$.

3.2 A DFT Wigner gradient flow model

To fully utilize the advantages of Wigner formalism that single function depicts the whole system, it is natural to consider energy minimization approaches for ground state calculations in Wigner formalism of many-body systems. In particular, we have the following energy functional,

$$E^{\text{KS}}[\rho] = \sum_{j=1}^{N_o} P_j \varepsilon_j - U_{\text{H}}[\rho] - \int_{\mathbb{R}^D} V_{\text{xc}}[\rho] \rho + E_{\text{xc}}[\rho]. \quad (30)$$

The corresponding minimization problem is written as

$$\begin{cases} \min & E^{\text{KS}}[\rho], \\ \text{s.t.} & \int_{\mathbb{R}^D} \rho = N_e. \end{cases} \quad (31)$$

where N_e is the electron number. The Wigner-Weyl of the energy operator gives

$$H_{\text{w}}^{\text{KS}}[\rho] f(\mathbf{x}, \mathbf{p}) = \frac{1}{2} \left(-\frac{\nabla_{\mathbf{x}}^2}{4} f(\mathbf{x}, \mathbf{p}) + |\mathbf{p}|^2 f(\mathbf{x}, \mathbf{p}) + \int_{\mathbb{R}^D} V_{\text{eig}}^{\text{KS}}[\rho](\mathbf{x}, \mathbf{p}') f(\mathbf{x}, \mathbf{p} - \mathbf{p}') d\mathbf{p}' \right), \quad (32)$$

where the last term corresponds to the one in Eq. (7) with the potential function in Eq. (9) replaced by $V_{\text{KS}}[\rho]$. Then the energy functional of the Kohn-Sham model is represented as

$$E_{\text{w}}^{\text{KS}}[f] = \frac{(2\pi)^D}{P_{\text{occ}}^{\text{cs}}} \iint_{\mathbb{R}^D \times \mathbb{R}^D} f(\mathbf{x}, \mathbf{p})^* H_{\text{w}}^{\text{KS}}[\rho] f(\mathbf{x}, \mathbf{p}) d\mathbf{x} d\mathbf{p} - E_{\text{ee}}[\rho] - \int_{\mathbb{R}^D} V_{\text{xc}}[\rho] \rho + E_{\text{xc}}[\rho], \quad (33)$$

with the density given by Eq. (4). Additionally, the constraint becomes

$$\iint_{\mathbb{R}^D \times \mathbb{R}^D} f(\mathbf{x}, \mathbf{p}) d\mathbf{x} d\mathbf{p} = N_e. \quad (34)$$

Suppose the second-order continuity of $V_{\text{xc}}[\rho]$ w.r.t. ρ , one can derive the following results by calculations for the Wigner function corresponding to the ground state of the Kohn-Sham model,

$$\begin{aligned} \frac{\delta E_{\text{w}}^{\text{KS}}[f]}{\delta f(\mathbf{x}, \mathbf{p})} &= (2\pi)^D H_{\text{w}}^{\text{KS}}[\rho] f(\mathbf{x}, \mathbf{p}) + \left(\frac{\delta U_{\text{H}}[\rho]}{\delta \rho(x)} + \frac{\delta V_{\text{xc}}[\rho]}{\delta \rho(x)} \right) \rho[f](x) \\ &\quad - \frac{\delta U_{\text{H}}[\rho]}{\rho[f](\mathbf{x})} \frac{\delta \rho[f](\mathbf{x})}{\delta f(\mathbf{x}, \mathbf{p})} - \left(\frac{\delta V_{\text{xc}}[\rho]}{\delta \rho[f](\mathbf{x})} \rho[f](\mathbf{x}) + V_{\text{xc}}[\rho](\mathbf{x}) \right) \frac{\delta \rho[f](\mathbf{x})}{\delta f(\mathbf{x}, \mathbf{p})} + \frac{\delta E_{\text{xc}}[\rho]}{\delta \rho[f](\mathbf{x})} \frac{\delta \rho[f](\mathbf{x})}{\delta f(\mathbf{x}, \mathbf{p})} \\ &= (2\pi)^D H_{\text{w}}^{\text{KS}}[\rho] f(\mathbf{x}, \mathbf{p}). \end{aligned} \quad (35)$$

Therefore, the Wigner gradient flow model for the Kohn-Sham model shares the form as one-body systems,

$$\begin{cases} \frac{\partial}{\partial t} f(\mathbf{x}, \mathbf{p}, t) = -(2\pi)^D H_{\text{w}}^{\text{KS}}[\rho] f(\mathbf{x}, \mathbf{p}, t), & t > 0, \\ \iint_{\mathbb{R}^D \times \mathbb{R}^D} f(\mathbf{x}, \mathbf{p}, t) d\mathbf{x} d\mathbf{p} = N_e, & t \geq 0. \end{cases} \quad (36)$$

4 Numerical scheme

Despite the advantage of the Wigner formalism that allows the depiction of the entire system by a single function, the problem dimensionality doubles compared to the original formulation. Therefore, efficient numerical scheme and discretization are crucial for ground state calculations in Wigner formalism. In Sect. 4.1, an operator splitting scheme is introduced, which validates the parallel implementations of the gradient flow model. Moreover, leveraging the structure of convolution operator in Eq. (32), the Fourier pseudo-spectral method is adopted for discretization in Sect. 4.2. Consequently, an efficient parallelizable algorithm is obtained, with the computational complexity $O(n_{\text{DoF}} \log n_{\text{DoF}})$.

4.1 Operator splitting method

With three operators

$$\mathcal{A}f(\mathbf{x}, \mathbf{p}, t) := -\frac{\nabla_{\mathbf{x}}^2}{4} f(\mathbf{x}, \mathbf{p}, t), \quad (37)$$

$$\mathcal{B}f(\mathbf{x}, \mathbf{p}, t) := |\mathbf{p}|^2 f(\mathbf{x}, \mathbf{p}, t), \quad (38)$$

$$\mathcal{C}[\rho]f(\mathbf{x}, \mathbf{p}, t) := \int_{\mathbb{R}^D} V_{\text{eig}}^{\text{KS}}[\rho](\mathbf{x}, \mathbf{p}') f(\mathbf{x}, \mathbf{p} - \mathbf{p}') d\mathbf{p}', \quad (39)$$

the evolution equation in (36) can be rewritten as

$$\frac{\partial}{\partial t} f(\mathbf{x}, \mathbf{p}, t) = -(\mathcal{A} + \mathcal{B} + \mathcal{C})f(\mathbf{x}, \mathbf{p}, t), \quad (40)$$

which can be split into the following three sub-equations in an alternating manner

$$\begin{cases} (\text{A}) \quad \frac{\partial}{\partial t} f(\mathbf{x}, \mathbf{p}, t) = -\mathcal{A}f(\mathbf{x}, \mathbf{p}, t) = \frac{\nabla_{\mathbf{x}}^2}{4} f(\mathbf{x}, \mathbf{p}, t), \\ (\text{B}) \quad \frac{\partial}{\partial t} f(\mathbf{x}, \mathbf{p}, t) = -\mathcal{B}f(\mathbf{x}, \mathbf{p}, t) = -|\mathbf{p}|^2 f(\mathbf{x}, \mathbf{p}, t), \\ (\text{C}) \quad \frac{\partial}{\partial t} f(\mathbf{x}, \mathbf{p}, t) = -\mathcal{C}[\rho]f(\mathbf{x}, \mathbf{p}, t) = -\int_{\mathbb{R}^D} V_{\text{eig}}^{\text{KS}}[\rho](\mathbf{x}, \mathbf{p}') f(\mathbf{x}, \mathbf{p} - \mathbf{p}') d\mathbf{p}'. \end{cases} \quad (41)$$

We employ a simple linearization and the well-known second-order Strang method [43],

$$f(\mathbf{x}, \mathbf{p}, t^{n+1}) = e^{-\mathcal{A}\Delta t/2} e^{-\mathcal{B}\Delta t/2} e^{-\mathcal{C}[c_{\text{nor}}[\rho^*]\rho^*]\Delta t} e^{-\mathcal{B}\Delta t/2} e^{-\mathcal{A}\Delta t/2} f(\mathbf{x}, \mathbf{p}, t^n) + O(\Delta t^2), \quad (42)$$

where t^n and t^{n+1} are two adjacent discrete moment, $\Delta t = t^{n+1} - t^n$,

$$\rho^*(\mathbf{x}) = \int_{\mathbb{R}^D} e^{-\mathcal{B}\Delta t/2} e^{-\mathcal{A}\Delta t/2} f(\mathbf{x}, \mathbf{p}, t^n) d\mathbf{p}, \quad c_{\text{nor}}[\rho] = \left(\int_{\mathbb{R}^D} \rho(\mathbf{x}) d\mathbf{x} \right)^{-1} \cdot N_e. \quad (43)$$

4.2 Fourier spectral collocation method

It is worth mentioning that variables decouple when solving sub-equation (A) and sub-equation (B) in Eq. (41), facilitating parallel implementation. Furthermore, the solution of sub-equation (C) actually corresponds to the independent evolution of Fourier coefficients, making the Fourier spectral collocation method an ideal choice for discretization. More specifically, we discretize each direction separately: (i) the \mathbf{x} -domain is either truncated or chosen as $\mathcal{X} = \prod_{j=1}^D [0, a_j]$, admitting a zero Dirichlet boundary condition or a periodic boundary condition; (ii) given the decay property of the Wigner function when $|\mathbf{p}| \rightarrow +\infty$, a simple nullification is adopted outside a sufficiently large \mathbf{p} -domain $\mathcal{P} = [-L/2, L/2]^D$. Consequently, the function $f(\mathbf{x}, \mathbf{p}, t)$ can be represented as

$$f(\mathbf{x}, \mathbf{p}, t) = \sum_{\nu_p \in \mathcal{I}_p} c_{\nu_p}(\mathbf{x}, t) \phi_{\nu_p}(\mathbf{p}) = \sum_{\nu_p \in \mathcal{I}_p} \sum_{\nu_x \in \mathcal{I}_x} c_{\nu_p, \nu_x}(t) \psi_{\nu_x}(\mathbf{x}) \phi_{\nu_p}(\mathbf{p}), \quad (44)$$

where x_j , p_j , $(\nu_x)_j$, $(\nu_p)_j$ and $(N_x)_j$ are the j -th components of \mathbf{x} , \mathbf{p} , ν_x , ν_p , and N_x respectively,

$$\psi_{\nu_x}(\mathbf{x}) = \exp \left(\sum_{j=1}^D 2\pi i (\nu_x)_j x_j / a_j \right), \quad (45)$$

$$\phi_{\nu_p}(\mathbf{p}) = \exp \left(\sum_{j=1}^D 2\pi i (\nu_p)_j (p_j - L/2) / L \right), \quad (46)$$

$$\mathcal{I}_x := \{\nu \in \mathbb{Z}^D : -(N_x)_j/2 \leq \nu_j < (N_x)_j/2, 1 \leq j \leq D\}, \quad (47)$$

$$\mathcal{I}_p := \{\nu \in \mathbb{Z}^D : -N_p/2 \leq \nu_j < N_p/2, 1 \leq j \leq D\}, \quad (48)$$

N_x and N_p stand for truncation orders in \mathbf{x} and \mathbf{p} direction, respectively. Then interpolation of the Wigner function into the solution space

$$\{\psi_{\nu_x}(\mathbf{x}) \phi_{\nu_p}(\mathbf{p}) : \nu_x \in \mathcal{I}_x, \nu_p \in \mathcal{I}_p\}, \quad (49)$$

has coefficients as follows,

$$c_{\nu_p}(\mathbf{x}, t) = \frac{1}{N_p^D} \sum_{\mu_p \in \mathcal{J}_p} f(\mathbf{x}, \mathbf{p}_{\mu_p}, t) \phi_{-\nu_p}(\mathbf{p}_{\mu_p}), \quad (50)$$

$$c_{\nu_x, \nu_p}(t) = \frac{1}{\prod_{j=1}^D (N_x)_j} \sum_{\mu_x \in \mathcal{J}_x} c_{\nu_p}(\mathbf{x}_{\mu_x}, t) \psi_{-\nu_x}(\mathbf{x}_{\mu_x}), \quad (51)$$

where $(\mu_x)_j$, $(\mu_p)_j$, $(\mu_x)_j a_j / (N_x)_j$ and $(\mu_p)_j L / N_p - L/2$ are the j -th component of μ_x , μ_p , \mathbf{x}_{μ_x} and \mathbf{p}_{μ_p} , respectively,

$$\mathcal{J}_x := \{\mu_x \in \mathbb{Z}^D : 0 \leq (\mu_x)_j < (N_x)_j, 1 \leq j \leq D\}, \quad (52)$$

$$\mathcal{J}_p := \{\mu_p \in \mathbb{Z}^D : 0 \leq (\mu_p)_j < N_p, 1 \leq j \leq D\}. \quad (53)$$

Remark 4.1. The degree of freedoms for the proposed method can be interpreted as the following equivalent sets in the sense of discrete Fourier transform and inverse discrete Fourier transform:

$$\{f(\mathbf{x}_{\mu_x}, \mathbf{p}_{\mu_p}, t)\}_{\mu_x \in \mathcal{J}_x, \mu_p \in \mathcal{J}_p}, \quad \{c_{\nu_p}(\mathbf{x}_{\mu_x}, t)\}_{\mu_x \in \mathcal{J}_x, \nu_p \in \mathcal{I}_p}, \quad \{c_{\nu_x, \nu_p}(t)\}_{\nu_x \in \mathcal{I}_x, \nu_p \in \mathcal{I}_p}. \quad (54)$$

Consequently, the evolution of sub-equations can be applied to one of these equivalent sets, with only one index involved and another one decouples. Therefore, the evolution of the gradient flow model can be efficiently accomplished by parallel implementations.

Now we consider the evolution for sub-equations separately,

- Sub-equation (A): Direct substitution of Eq. (44) and the orthogonality of $\{\phi_{\nu_p}\}_{\nu_p \in \mathcal{I}_p}$ imply that

$$\frac{\partial}{\partial t} c_{\nu_p}(\mathbf{x}, t) = \frac{\nabla_{\mathbf{x}}^2}{4} c_{\mu_p}(\mathbf{x}, t), \quad \mu_p \in \mathcal{I}_p, \quad (55)$$

which is equivalent to

$$\frac{d}{dt} c_{\mu_x, \mu_p}(t) = -\pi^2 \sum_{j=1}^D \left(\frac{(\nu_x)_j}{a_j} \right)^2 c_{\mu_x, \mu_p}(t), \quad \mu_x \in \mathcal{I}_x, \mu_p \in \mathcal{I}_p. \quad (56)$$

Therefore the numerical solution can be explicitly given as

$$c_{\mu_x, \mu_p}(t^{n+1}) = \exp \left(-\pi^2 \Delta t \sum_{j=1}^D \left(\frac{(\nu_x)_j}{a_j} \right)^2 \right) c_{\mu_x, \mu_p}(t^n), \quad \mu_x \in \mathcal{I}_x, \mu_p \in \mathcal{I}_p. \quad (57)$$

- Sub-equation (B): We consider the effect acts on the first set of (54),

$$\frac{\partial}{\partial t} f(\mathbf{x}_{\mu_x}, \mathbf{p}, t) = -|\mathbf{p}|^2 f(\mathbf{x}_{\mu_x}, \mathbf{p}, t), \quad \mu_x \in \mathcal{J}_x, \quad (58)$$

whose solution is

$$f(\mathbf{x}_{\mu_x}, \mathbf{p}_{\mu_p}, t^{n+1}) = \exp(-|\mathbf{p}_{\mu_p}|^2 \Delta t) f(\mathbf{x}_{\mu_x}, \mathbf{p}_{\mu_p}, t^n), \quad \mu_x \in \mathcal{J}_x, \mu_p \in \mathcal{J}_p. \quad (59)$$

- Sub-equation (C): Suppose $V_{\text{eig}}^{\text{KS}}[\rho](\mathbf{x}, \mathbf{p})$ decay to zero outside some \mathbf{p} -domain, it follows Poisson summation formula that

$$\begin{aligned} \mathcal{C}[\rho] f(\mathbf{x}, \mathbf{p}, t) &\approx \left(\frac{\Delta y}{2\pi} \right)^D \sum_{\mu \in \mathbb{Z}^3} S_{V_{\text{KS}}[\rho]}(\mathbf{x}, \mathbf{y}_\mu) \int_{\mathcal{P}} \exp(-i\mathbf{p}' \cdot \mathbf{y}) \sum_{\nu_p \in \mathcal{I}_p} c_{\nu_p}(\mathbf{x}, t) \phi_{\nu_p}(\mathbf{p}) d\mathbf{p} \\ &= \sum_{\nu_p \in \mathcal{I}_p} S_{V_{\text{KS}}[\rho]}(\mathbf{x}, \mathbf{y}_{-\nu_p}) c_{\nu_p}(\mathbf{x}, t) \phi_{\nu_p}(\mathbf{p}), \end{aligned} \quad (60)$$

where it requires that $L \cdot \Delta y = 2\pi$ [48], and \mathbf{y}_{ν_p} has j -th component $(\nu_p)_j \Delta y$. Therefore, the sub-equation (C) can be converted to

$$\frac{\partial}{\partial t} c_{\nu_p}(\mathbf{x}, t) = S_{V_{\text{KS}}[\rho]}(\mathbf{x}, \mathbf{y}_{-\nu_p}) c_{\nu_p}(\mathbf{x}, t), \quad \nu_p \in \mathcal{I}_p. \quad (61)$$

With simple linearization, one can obtain an explicit expression of the solution as

$$c_{\nu_p}(\mathbf{x}_{\mu_x}, t^{n+1}) = \exp \left(-\Delta t S_{V_{\text{KS}}[c_{\text{nor}} c_0^n]}(\mathbf{x}_{\mu_x}, \mathbf{y}_{-\nu_p}) \right) c_{\nu_p}(\mathbf{x}_{\mu_x}, t^n), \quad \mu_x \in \mathcal{J}_x, \nu_p \in \mathcal{I}_p, \quad (62)$$

where c_{nor} stands for the normalization coefficient such that $\int_{\mathcal{X}} c_{\text{nor}} c_0$ recovers the electron number.

Moreover, the concerned quantities, i.e., density and energy can be expressed as

$$\rho(\mathbf{x}, t) = L^D c_0(\mathbf{x}, t), \quad (63)$$

$$E(t) = \frac{L^{D-1}}{2} \sum_{\nu_p \in \mathcal{I}_p^0} \frac{L^3}{2\pi^2 |\nu_p|^2 + 12\delta_{0,|\nu_p|}/D} |\mathcal{X}| c_{0, \nu_p}(t), \quad (64)$$

with

$$\mathcal{I}_p^0 := \{\nu_p \in \mathcal{I}_p : \#\{j : (\nu_p)_j = 0\} \geq 2\}. \quad (65)$$

Finally, denoting the unknowns in (54) as F_μ , $C_{\nu, \mu}$, C_ν , respectively, the flowchart of the proposed numerical method for solving the DFT Wigner gradient flow model is presented in the algorithm below,

Algorithm 1 DFT Wigner gradient flow model solving the ground state Wigner function.

Require: Initial guess $C_{\nu,\mu}^{\text{init}}$, time step size dt , iteration step for single test N_{test} , maximum test step N_{test}^{\max} , tolerance Tol .

Ensure: Fourier coefficients $C_{\nu,\mu}$ for the ground state Wigner function, ground state density ρ_{out} and energy E_{out} .

- 1: Set $C_{\nu,\mu} = C_{\nu,\mu}^{\text{init}}$, calculate ρ^0 by (63).
- 2: **for** $n = 1 : N_{\text{test}}^{\max}$ **do**
- 3: **for** $n_{\text{evolve}} = 1 : N_{\text{test}}$ **do**
- 4: Attain C_{ν} by applying the discrete Fourier transform to $C_{\nu,\mu}$ w.r.t. variable \mathbf{x}_{μ} , update C_{ν} following (57) with time step size $dt/2$, recover $C_{\nu,\mu}$ by the inverse discrete Fourier transform.
- 5: Attain F_{μ} by applying the discrete Fourier transform to $C_{\nu,\mu}$ w.r.t. variable \mathbf{p}_{μ} , update F_{μ} following (59) with time step size $dt/2$, recover $C_{\nu,\mu}$ by the inverse discrete Fourier transform.
- 6: Calculate density $S_{V_{\text{KS}}[c_{\text{nor}}c_0^*]}(\mathbf{x}_{\mu_x}, y_{\nu_p})$ with $C_{0,\mu}$, update $C_{\nu,\mu}$ following (62) with time step size dt .
- 7: Attain F_{μ} by applying the discrete Fourier transform to $C_{\nu,\mu}$ w.r.t. variable \mathbf{p}_{μ} , update F_{μ} following (59) with time step size $dt/2$, recover $C_{\nu,\mu}$ by the inverse discrete Fourier transform.
- 8: Attain C_{ν} by applying the discrete Fourier transform to $C_{\nu,\mu}$ w.r.t. variable \mathbf{x}_{μ} , update C_{ν} following (57) with time step size $dt/2$, recover $C_{\nu,\mu}$ by the inverse discrete Fourier transform.
- 9: **end for**
- 10: Calculate density ρ^n and energy E^n by (63) and (64), evaluate error $e_{\rho} = \|\rho^n - \rho^{n-1}\|_2$.
- 11: **if** $e_{\rho} < Tol$ **then**
- 12: Set $\rho^{\text{out}} = \rho^n$, $E^{\text{out}} = E^n$.
- 13: Break.
- 14: **end if**
- 15: **end for**

Remark 4.2. It can be observed that each evolution depends on only one variable, which enables the acceleration by parallel calculations according to another one.

Remark 4.3. Since the evolution of each sub-equation has an explicit expression, the computational complexity of the Fourier transform and inverse Fourier transform dominates in the evolution of single time step. Hence, the computational cost of single time step is $O(N_{\text{DoF}} \log N_{\text{DoF}})$ for degree of freedom number N_{DoF} .

5 Numerical results

In this section, two toy models are presented to validate the proposed method. Firstly, the periodic extension of one-dimensional delta-interacting Hooke's atom is examined, where a system with up to 2^{21} electron is tested. Subsequently, a three-dimensional system is considered for investigating the effect of Coulomb interaction. The three-dimensional system is generated by the periodic extension of three-dimensional Hooke's atom, subjecting to external potential and Hartree potential. Moreover, a system with central absence is exhibited for the further illustration of the descriptive capability of the Wigner formalism. Anticipated spectral accuracy can be successfully observed in all the computations, while multiple-cell simulations recover the desired errors compared to single-cell simulations. These examples demonstrate the potential applications of our approach to large-scale systems and systems with defects.

In particular, the models in this section can be regarded as periodic extensions of quantum systems within a single cell subjecting to periodic boundary conditions. Consequently, the system on multiple cells can be easily obtained by extending both domain and potential setup periodically. Therefore, the DFT systems within a single cell will be introduced in the following context.

All numerical experiments are implemented using a workstation, with two AMD Epyc 7713 Processor 64 Core 2.0GHz 256MB L3 Cache (total 128 cores), 881GB memory. The operation system is Ubuntu 22.04.

5.1 1-D delta-interacting Hooke's atom

In this example, simulations are conducted on both single-cell and quadruple-cell systems to validate the proposed method. The results are summarized as Fig. 5.1, Fig. 5.2 for the single-cell simulations and Fig. 5.3 for the quadruple-cell simulations. Additionally, the numerical results in both the Schrödinger formalism and Wigner formalism with sufficient truncation order are employed as the numerical reference. Moreover, a comparison between the Wigner results in multiple-cell simulations and those in single-cell simulations is presented in Table 5.1.

Consider a one-dimensional two-particle system

$$\left(-\frac{1}{2} \frac{\partial}{\partial x_1} - \frac{1}{2} \frac{\partial}{\partial x_2} + V_{\text{ext}}(x_1) + V_{\text{ext}}(x_2) + V_{\text{ee}}(x_1 - x_2) \right) \Psi(x_1, x_2) = E \Psi(x_1, x_2), \quad (66)$$

where

$$V_{\text{ext}}(x) = \frac{1}{2}x^2, \quad V_{\text{ee}}(x) = \delta(x). \quad (67)$$

This system can be approximated by the Kohn-Sham model

$$\left(-\frac{1}{2} \frac{d^2}{dx^2} + V_{\text{KS}}[\rho](x) \right) \psi_j = \varepsilon_j \psi_j(x), \quad (68)$$

where

$$V_{\text{KS}}[\rho](x) = V_{\text{ext}}(x) + V_{\text{H}}[\rho](x) + V_{\text{xc}}[\rho](x), \quad (69)$$

with

$$V_{\text{H}}[\rho](x) = \frac{\delta U[\rho]}{\delta \rho(x)}, \quad \text{and} \quad V_{\text{xc}}[\rho](x) = \frac{\delta(E_{\text{x}}^{\text{LDA}}[\rho] + E_{\text{c}}^{\text{LDA}}[\rho])}{\delta \rho(x)}. \quad (70)$$

Here

$$U_{\text{H}}[\rho] = \frac{1}{2} \int_{\mathcal{X}} \rho(x)^2 dx, \quad \text{and} \quad E_{\text{x}}^{\text{LDA}}[\rho] = -\frac{1}{4} \int_{\mathcal{X}} \rho(x)^2 dx, \quad (71)$$

while the correlation energy is approximated by the local density approximation in [25]

$$E_{\text{c}}^{\text{LDA}}[\rho] = \int_{\mathcal{X}} \frac{a\rho(x)^3 + b\rho(x)^2}{\rho(x)^2 + d\rho(x) + e} dx, \quad (72)$$

where $a = -1/24$, $b = -0.00436143$, $d = 0.252758$ and $e = 0.0174457$.

We begin by investigating simulations conducted on a single cell. In particular, simulations are performed with varying \mathbf{x} truncation orders $M = 8, 16, 24, 32, 40, 48, 56$ and fixed \mathbf{p} truncation orders $N = 128$. Using the numerical results in the Schrödinger formalism with $M = 128$ as the reference, the decay behavior of errors are is illustrated in the left figure of Fig. 5.1. Additionally, the error decay with respect to the Wigner reference when $M = N = 128$ is exhibited in the right figure of Fig. 5.1. Conversely, by fixing truncation order in the \mathbf{x} direction as $M = 128$, Wigner simulations with truncation orders in the \mathbf{p} direction as $N = 24, 32, 40, 48, 56, 64, 72$ are accomplished, with error decay depicted in Fig. 5.2. Similarly, the Schrödinger/Wigner reference is considered in the left/right figure of Fig. 5.2, respectively. Furthermore, the behavior of each component of the total energy is presented separately.

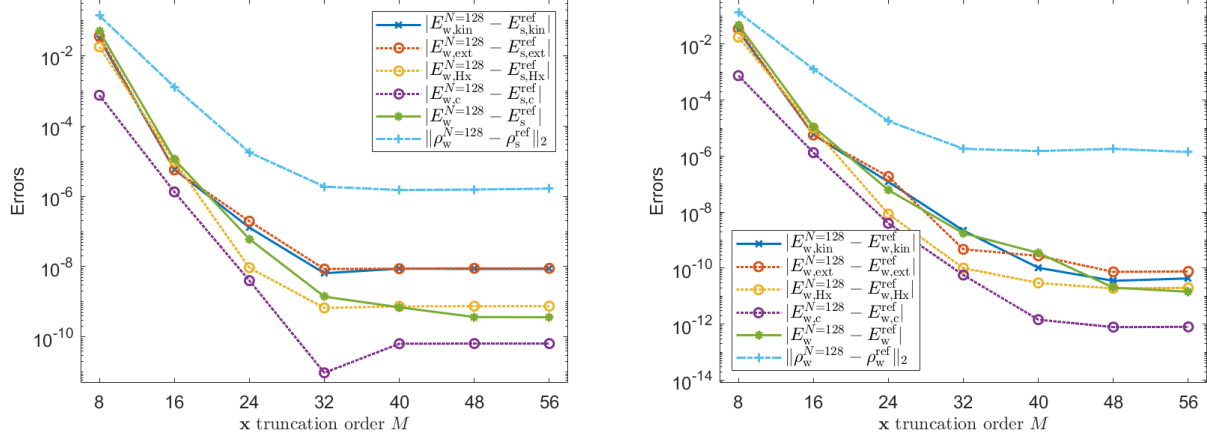


Figure 5.1: Decay of errors w.r.t. Schrödinger (left)/Wigner (left) reference for different \mathbf{x} truncation order in single-cell simulations.

It can be found in Fig. 5.1 that (i) The convergence of density to both the Schrödinger reference and Wigner reference, as well as the convergence of energy and energy components, can be obtained in all the simulations. (ii) Spectral convergence with respect to \mathbf{x} truncation order M to both the Schrödinger reference and Wigner reference is evident across all the computations. (iii) The error decay of energy components $E_{w,ext}^N$, $E_{w,kin}^N$ and $E_{w,c}^N$ exhibits similar behavior to the density errors, resulting from the fact that these components are determined by the density. (iv) Since the kinetic energy is a functional of all the coefficient functions, its errors show the worst decay behavior compared to others. Particularly, the error of kinetic energy finds no improvement when the truncation order is sufficiently large (e.g., larger than 40), due to the absence of higher coefficient functions. In such cases, discretization errors in the \mathbf{p} direction become dominant.

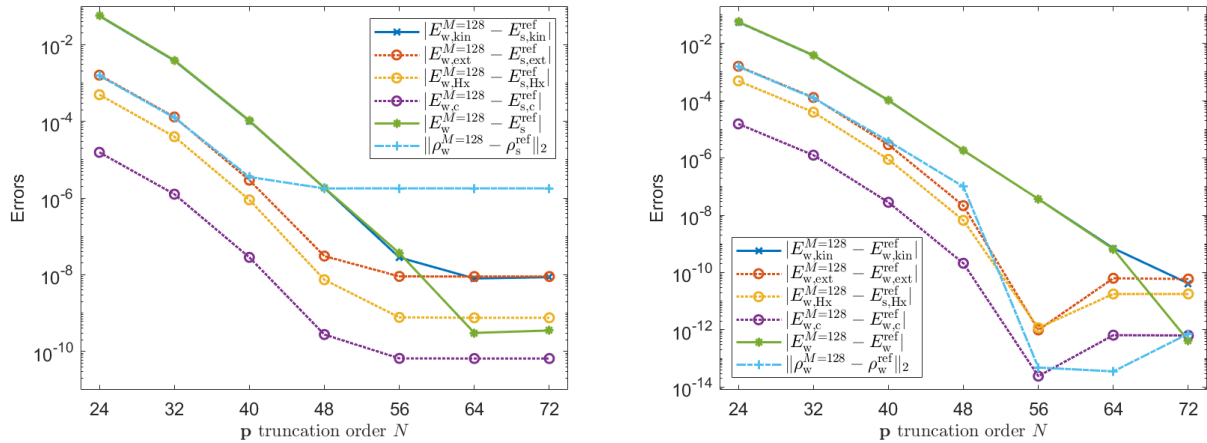


Figure 5.2: Decay of errors w.r.t. Schrödinger (left)/Wigner (left) reference for different \mathbf{p} truncation order in single-cell simulations.

The numerical observations in Fig. 5.2 can be summarized as follows: (i) Spectral convergence with respect to \mathbf{p} truncation order N to both Schrödinger reference and Wigner reference can be obtained in all the simulations. (ii) The errors of density-determined energy components exhibit a similar behavior to the density errors. (iii) Compared to the gentle behavior with sufficient large N using the Schrödinger reference, the results with respect to the Wigner reference show a smooth error decay. This is attributed to the use of numerical results with the same \mathbf{x} truncation order $M = 128$.

Fig. 5.3 illustrates the numerical outcomes of simulations conducted on quadruple cells. Specifically, the simulations encompass the \mathbf{x} truncation orders ranging from $M = 32$ to $M = 224$ with increments of 32, while maintaining a fixed \mathbf{p} truncation order of $N = 128$. Additionally, results for $M = 256$ with $N = 24, 32, 40, 48, 56, 64, 72$ are presented. Throughout these calculations, the Schrödinger reference

with $M = 512$ and the Wigner reference with $M = 512, N = 128$ are employed to demonstrate convergence behavior. Similarly, the components of total energy are depicted in the figures, facilitating a deeper investigation of the numerical findings.

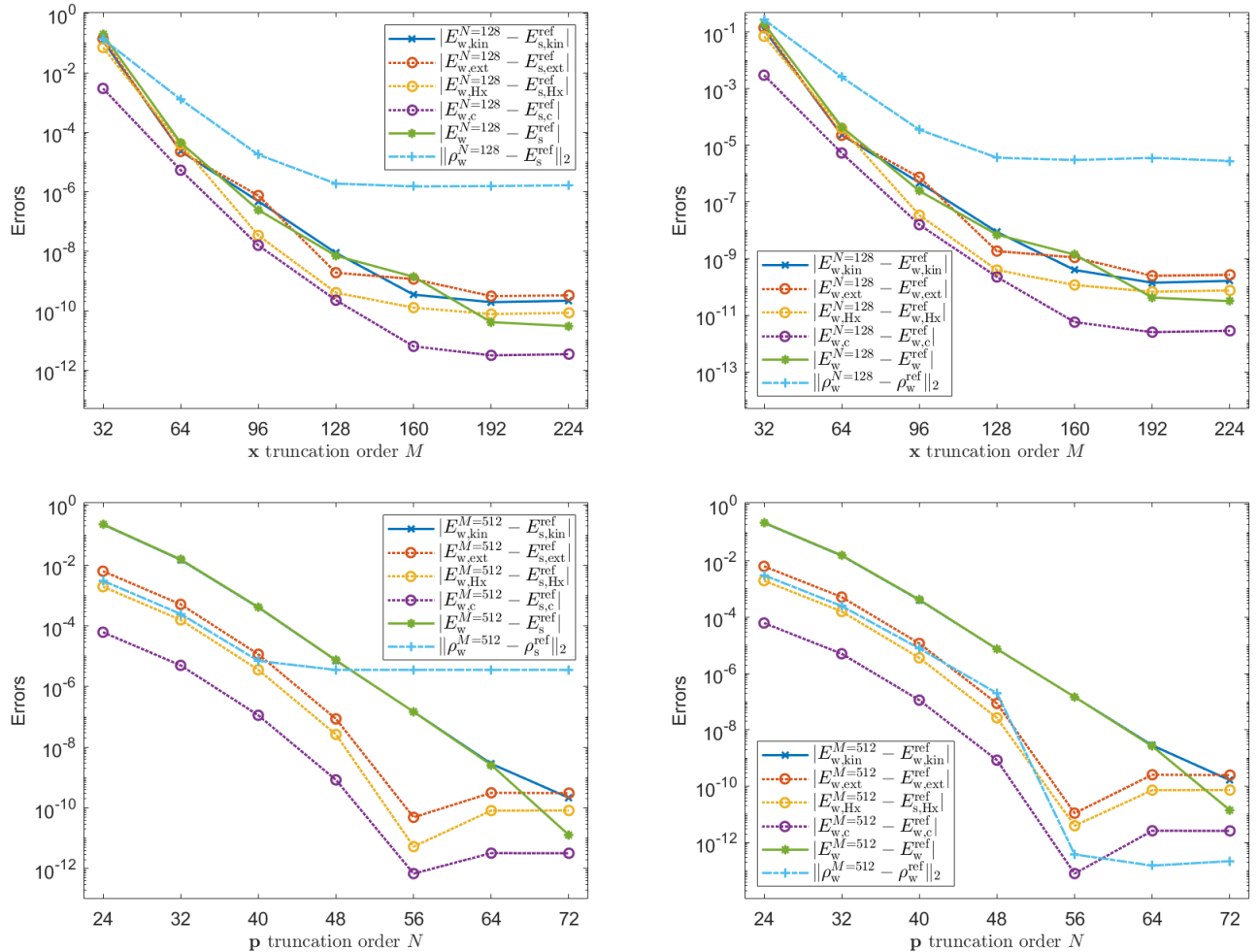


Figure 5.3: Decay of errors w.r.t. Schrödinger (left)/Wigner (left) reference for different \mathbf{x} (top) \mathbf{p} (bottom) truncation order in quadrupole cell simulations.

Similar observations can be obtained in Fig. 5.3. (i) The spectral convergence to the reference in both the \mathbf{x} and \mathbf{p} direction can be found in the computations. (ii) The errors of density-determined energy components exhibit a similar behavior to the density errors. (iii) On the contrary, the kinetic energy depends on all coefficient functions, resulting in a gentle behavior of kinetic errors in the top figures when the truncation order is sufficiently large. (iv) Smooth convergence to the reference can be observed in the bottom right figure due the use of numerical Wigner results with the same \mathbf{x} truncation order.

Finally, employing the numerical results in single-cell simulations as a reference, the errors of multiple-cell simulations are presented in Table 5.1. In detail, the cell number $n_{\text{cell}} = 1, 2, 4, 8, 16, 32, 64, 2^{20}$ are considered, whose corresponding degree of freedom numbers are shown in the row n_{DoF} . The truncation orders are set as $M = 32n_{\text{cell}}$ and $N = 32$. The row E_w lists the energy of the corresponding calculation, while $E_{w,\text{avg}}$ provides the energy per cell of multiple-cell simulations. The reference energies E_s^{ref} , E_w^{ref} are the corresponding numerical energies. And the reference densities ρ_s^{ref} and ρ_w^{ref} are generated by the periodic extension of the one in the Schrödinger formalism with $M = 128$ and the one in the Wigner formalism with $M = N = 128$, respectively. To provide a more comprehensive demonstration of the errors, the average energy errors are presented in the third and fourth rows. Additionally, due to the use of L_2 norm, the average density errors, divided by the square root of cell number, are shown in the last two rows.

Table 5.1: Errors of multiple cell simulations

| n_{cell} | 1 | 2 | 4 | 8 | 16 | 32 | 64 | 2^{20} |
|---|----------|----------|----------|----------|----------|----------|----------|------------|
| n_{DoF} | 1024 | 2048 | 4096 | 8192 | 16384 | 32768 | 65536 | 33554432 |
| E_w | 1.31 | 2.62 | 5.24 | 10.48 | 20.96 | 41.92 | 83.83 | 1373484.49 |
| $ E_{w,\text{avg}} - E_s^{\text{ref}} $ | 3.91e-03 |
| $ E_{w,\text{avg}} - E_w^{\text{ref}} $ | 3.91e-03 |
| $\ \rho_w - \rho_s^{\text{ref}}\ _2$ | 1.25e-04 | 1.77e-04 | 2.50e-04 | 3.54e-04 | 5.00e-04 | 7.07e-04 | 1.00e-03 | 2.67e-01 |
| $\ \rho_w - \rho_s^{\text{ref}}\ _2 / \sqrt{n_{\text{cell}}}$ | 1.25e-04 | 1.71e-04 |
| $\ \rho_w - \rho_w^{\text{ref}}\ _2$ | 1.25e-04 | 1.77e-04 | 2.50e-04 | 3.54e-04 | 5.01e-04 | 7.08e-04 | 1.00e-03 | 2.67e-01 |
| $\ \rho_w - \rho_w^{\text{ref}}\ _2 / \sqrt{n_{\text{cell}}}$ | 1.25e-04 | 1.71e-04 |

It is revealed in Table 5.1 that almost all multiple-cell simulations yield identical average energy errors and average density errors, at least to 4 decimal places. Remarkably, the calculation on 2^{20} cells produces average energy error and density error of the same order, which also achieves a satisfactory accuracy (less than 1×10^{-3}). Conversely, to deliver a similar average error for larger systems, the increase of the DoF number merely grows linearly w.r.t. the cell number, resulting in an almost linear growth of computational complexity for a single iteration. It also is desired mentioned that only a single Wigner function is computed in each simulation, underscoring the descriptive capability of the Wigner formalism and its potential to large scale simulations.

5.2 3-D Hooke's atom

In this sub-section, a three-dimensional system is examined to explore the impact of Coulomb interaction. Firstly, single-cell simulations are accomplished for testifying the spectral accuracy of the Fourier pseudo-spectral method. The results of these computations are collected as Fig. 5.4 and Fig. 5.5. Subsequently, both the energy errors and density errors for multiple-cell simulations are exhibited in Table 5.2, underscoring the descriptive capability of the Wigner formalism. Moreover, a comparison of density distribution between $3 \times 3 \times 3$ -cell simulations and those with central absence is demonstrated in Fig. 5.6, which illustrates the potential applications of our approach for simulating systems with defects.

Particularly, for single-cell system we have

$$\left(-\frac{1}{2} \nabla^2 + V_{\text{ext}}(\mathbf{r}) + V_{\text{H}}[\rho](\mathbf{r}) \right) \psi_j(\mathbf{r}) = \varepsilon_j \psi_j(\mathbf{r}), \quad (73)$$

where $\mathbf{r} = (x, y, z)$ stands for three-dimensional coordinates,

$$V_{\text{ext}}(\mathbf{r}) = \frac{1}{2} |\mathbf{r}|^2, \quad (74)$$

$$V_{\text{H}}(\mathbf{r}) = \int_{\mathcal{X}} \frac{\rho(\mathbf{r}')}{|\mathbf{r} - \mathbf{r}'|} d\mathbf{r}'. \quad (75)$$

For simplicity, uniform truncation order across all the directions are adopted for the discretization of \mathbf{x} and \mathbf{p} domains, respectively. We begin with single-cell simulations using \mathbf{x} truncation order $M = 8, 10, 12, 14, 16, 20$ and \mathbf{p} truncation order $N = 32$, whose results are demonstrated in Fig. 5.4. Conversely, simulations with $M = 32$ and $N = 20, 24, 28, 32, 36$ are also conducted. The Schrödinger results with $M = 64$ and the Wigner results with $M = N = 48$ are employed as the reference. Similarly,

the error behavior of energy components $E_{w,kin}$, $E_{w,ext}$ and $E_{w,H}$ are presently separately for further analysis.

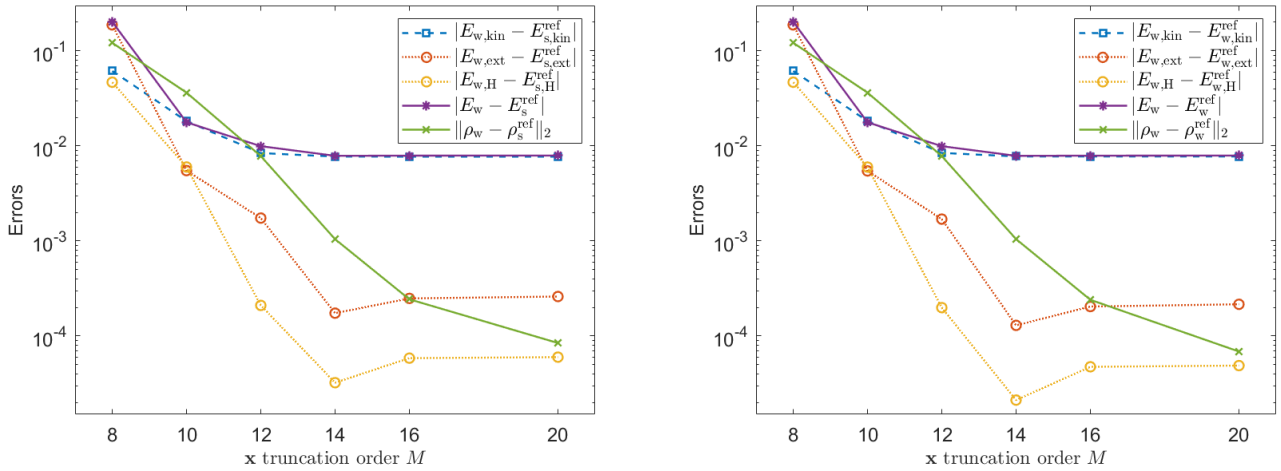


Figure 5.4: Decay of errors w.r.t. Schrödinger (left)/Wigner (left) reference for different \mathbf{x} truncation order in single cell simulations.

One can observe in Fig. 5.4 that (i) Spectral convergence with respect to M to both the Schrödinger and Wigner reference can be obtained. (ii) The energy error of density-determined energy components exhibit a similar behavior to the density errors. (iii) Increasing M shows no improvement of the kinetic energy errors when M is large enough (e.g., $M > 32$), resulting from the fact that the discretization error in \mathbf{p} direction dominates in these situations.

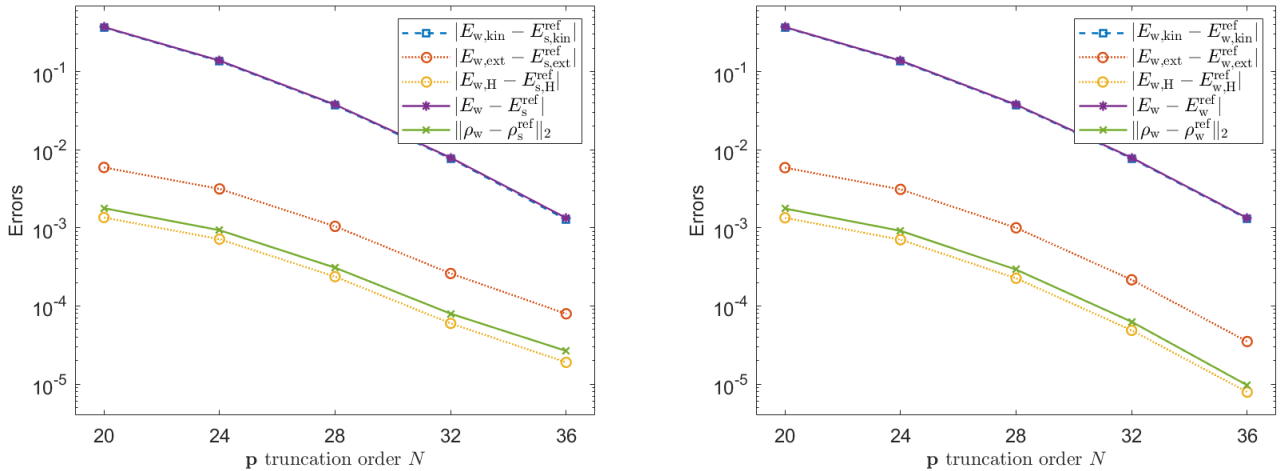


Figure 5.5: Decay of errors w.r.t. Schrödinger (left)/Wigner (left) reference for different \mathbf{p} truncation order in single cell simulations.

It can be found in Fig. 5.5 that the density errors, energy errors and the errors of energy components all demonstrate the spectral convergence with respect to \mathbf{p} truncation order N .

Next we consider multiple-cell simulations, whose results are concluded as the following table. In each simulation, the \mathbf{x} truncation order is employed as the corresponding multiple of 16, i.e., taking $M_x = 16n_x^{\text{multi}}$, $M_y = 16n_y^{\text{multi}}$, $M_z = 16n_z^{\text{multi}}$ for the cell type $n_x^{\text{multi}} \times n_y^{\text{multi}} \times n_z^{\text{multi}}$, with the \mathbf{p} truncation order $N = 32$. The reference energy and density are obtained from the periodic extension of the Schrödinger results with $M = 64$ and the Wigner results with $M = N = 48$. In Table 5.2, the row E_w lists the energies of multiple-cell simulations, the row $e_E^{\text{s,avg}}$ and the row $e_E^{\text{w,avg}}$ list the energy errors per cell with respect to the Schrödinger and Wigner reference. Additionally, the row e_ρ^{s} and the row e_ρ^{w} correspond to the density errors with respect to the reference. Similarly, the row $e_\rho^{\text{s,avg}}$ and the row $e_\rho^{\text{w,avg}}$ exhibit the average density errors in the sense of dividing by the square root of cell number.

Table 5.2: Errors of multiple cell simulations

| cell type | $1 \times 1 \times 1$ | $3 \times 1 \times 1$ | $1 \times 3 \times 1$ | $1 \times 1 \times 3$ | $2 \times 2 \times 1$ | $2 \times 1 \times 2$ | $1 \times 2 \times 2$ | $2 \times 2 \times 2$ | $3 \times 3 \times 3$ |
|-------------------------|-----------------------|-----------------------|-----------------------|-----------------------|-----------------------|-----------------------|-----------------------|-----------------------|-----------------------|
| n_{DoF} | 1.34e08 | 4.03e08 | 4.03e08 | 4.03e08 | 5.37e08 | 5.37e08 | 5.37e08 | 1.07e09 | 3.62e09 |
| E_w | 3.49 | 10.46 | 10.46 | 10.46 | 13.95 | 13.95 | 13.95 | 27.90 | 94.15 |
| $e_E^{\text{s,avg}}$ | 7.90e-04 |
| $e_E^{\text{w,avg}}$ | 7.90e-04 |
| e_ρ^{s} | 2.43e-04 | 4.21e-04 | 4.21e-04 | 4.21e-04 | 4.85e-04 | 4.85e-04 | 4.85e-04 | 6.86e-04 | 1.30e-03 |
| $e_\rho^{\text{s,avg}}$ | 2.43e-04 | 2.43e-04 | 2.43e-04 | 2.43e-04 | 2.42e-04 | 2.42e-04 | 2.42e-04 | 2.42e-04 | 2.50e-04 |
| e_ρ^{w} | 2.40e-04 | 4.16e-04 | 4.16e-04 | 4.16e-04 | 4.80e-04 | 4.80e-04 | 4.80e-04 | 6.78e-04 | 1.28e-03 |
| $e_\rho^{\text{w,avg}}$ | 2.40e-04 | 2.46e-04 |

It can be found in Table 5.2 that multiple-cell simulations yield consistent average energy errors and average density errors in all the cell type. Moreover, all the average errors are less than 1.0×10^{-3} , deliver a desired accuracy. Similarly, a almost linear increase of the computational complexity for a single iteration, resulting from the linear growth of the DoF number w.r.t. the system scale, delivers a comparable average error as the single cell case. It is worth mentioning that the Wigner formalism enables the description of the entire system by a single Wigner function regardless of the system size. Moreover, in our method, the computational cost of single evolution increases almost linearly with the system size. This underscore the potential of our approach for large-scale simulations.

Finally, the visualization results of $3 \times 3 \times 3$ cell simulations are exhibited in Fig. 5.6. The density distribution of the system without central cell arrangement is also included. In particular, the \mathbf{x} truncation order is employed as $M_x = M_y = M_z = 48$, and the \mathbf{p} truncation order is $N = 16$ in all directions. In the simulation corresponding to the left figure of Fig. 5.6, each sub-cell subjects to the external potential $V_{i_{\text{cell}}}(\mathbf{r}) = |\mathbf{r} - \mathbf{r}_{\text{center}}^{i_{\text{cell}}}|^2/2$, where i_{cell} is the cell index, and $\mathbf{r}_{\text{center}}^{i_{\text{cell}}}$ is the center position of this sub-cell. On the contrary, the simulation shown in right figure features the absence of the external potential in center sub-cell, resulting in the electron number 54 compared to the one 56 in the left figure. To better illustrate the density distribution, we consider the isosurfaces for the density $\rho = 0.01 + 0.005j$ with $0 \leq j \leq 6$, clipped by the plane $y = z$.

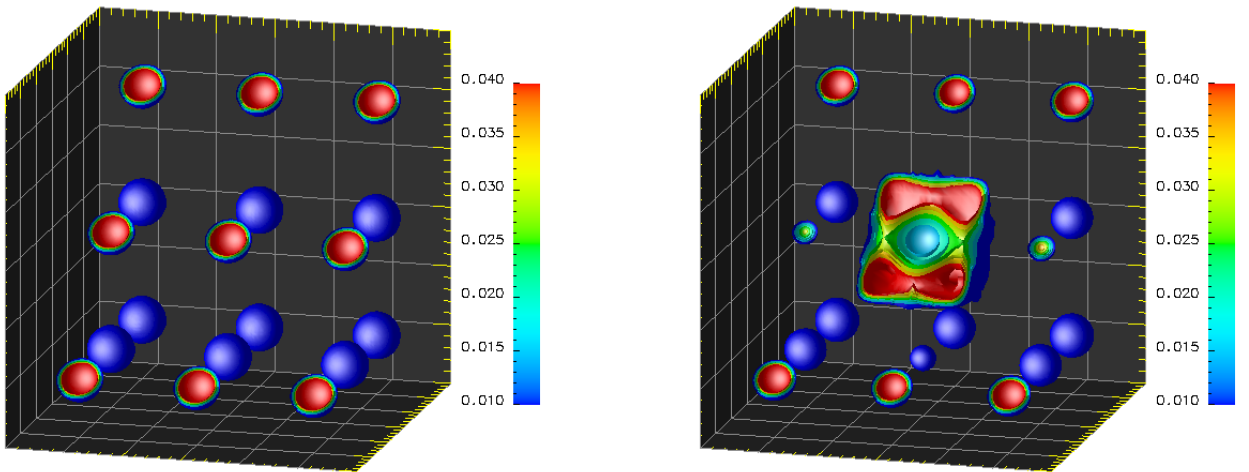


Figure 5.6: Density distribution of Wigner results for $3 \times 3 \times 3$ cells (left) and $3 \times 3 \times 3$ with central absence (right).

It can be observed in Fig. 5.6 that (i) in the left figure, the density within each sub-cell exhibits

the same distribution, which is symmetric with respect to the sub-cell center. (ii) Similarly, the density distribution in sub-cells of the right figure also displays symmetric behavior. (iii) Specially, due to the absence of external potential in the right figure, only few density is present around the cell center of the entire system. Additionally, the sub-cells near to the center sub-cell also exhibit smaller density distributions. It is worth mentioning that the only difference between the numerical simulations for these two figures is the external potential and the electron number. Therefore, Wigner computations are expected to offer a more straightforward description of complex systems in numerical calculations. This arises from the feature that Kohn-Sham orbitals are expressed as an ensemble in the corresponding Wigner function within the Wigner formalism.

6 Conclusion

In this paper, a gradient flow model is derived for Wigner ground state calculation of many-body system in the context of density functional theory. In particular, a gradient flow model for one-body systems is firstly derived and then extended to many-body systems within the framework of density functional theory. To enhance computational efficiency, an operator splitting scheme and the Fourier pseudo-spectral method are introduced for numerical simulations, which delivers a parallelizable algorithm with $O(n_{\text{DoF}} \log n_{\text{DoF}})$ computational cost for a single evolution step. Two toy models, based on the periodic extensions of two-body systems, are presented to demonstrate the efficacy of our approach, encompassing a one-dimensional delta-interacting example with a local density approximation and a three-dimensional system with Coulomb interaction. Spectral accuracy can be successfully observed in computations, while multiple-cell simulations recover the desired errors compared to the single-cell simulations. Moreover, the use of the same setup in \mathbf{p} space for multi-cell calculations results in an almost linear increase in computational complexity for a single iteration, demonstrating the potential of the proposed method for simulating large-scale systems and systems with defects.

As for future work, there are two primary avenues of exploration. On the one hand, we aim to extend our simulations to encompass more general systems, such as complex molecular systems. On the other hand, we aim to address the current limitations in the size of the discretized system required for accurately representing three-dimensional systems. To enhance the efficiency of our method, we will explore numerical strategies, such as selectively ignoring certain coefficient functions to reduce computational resource requirements per iteration. Alternatively, we may explore the Grad moment method, which possesses a straightforward expressions of both density and energy.

References

- [1] Anton Arnold. A mixed spectral-collocation and operator splitting method for the Wigner-Poisson equation. In *Mathematics of Computation 1943-1993: A Half-Century of Computational Mathematics: Mathematics of Computation 50th Anniversary Symposium, August 9-13, 1993, Vancouver, British Columbia*, volume 48, page 249. American Mathematical Society, 1994.
- [2] Anton Arnold and Christian Ringhofer. Operator splitting methods applied to spectral discretizations of quantum transport equations. *SIAM Journal on Numerical Analysis*, 32(6):1876–1894, 1995.
- [3] Denys I. Bondar, Andre G. Campos, Renan Cabrera, and Herschel A. Rabitz. Efficient computations of quantum canonical Gibbs state in phase space. *Physical Review E*, 93:063304, Jun 2016.
- [4] Amartya Bose and Nancy Makri. Coherent state-based path integral methodology for computing the Wigner phase space distribution. *The Journal of Physical Chemistry A*, 123(19):4284–4294, 2019. PMID: 30986061.
- [5] Zhenning Cai, Yuwei Fan, Ruo Li, and Tiao Lu. Quantum hydrodynamic model of density functional theory. *Journal of Mathematical Chemistry*, 51:1747–1771, 2013.

[6] William B. Case. Wigner functions and Weyl transforms for pedestrians. *American Journal of Physics*, 76(10):937–946, 2008.

[7] Zhenzhu Chen, Sihong Shao, and Wei Cai. A high order efficient numerical method for 4-D Wigner equation of quantum double-slit interferences. *Journal of Computational Physics*, 396:54–71, 2019.

[8] Jens Peder Dahl. Moshinsky atom and density functional theory - A phase space view. *Canadian Journal of Chemistry*, 87(7):784–789, 2009.

[9] Jens Peder Dahl and Michael Springborg. Wigner’s phase space function and atomic structure I. The hydrogen atom ground state. *Molecular Physics*, 47(5):1001–1019, 1982.

[10] Sambit Das, Bikash Kanungo, Vishal Subramanian, Gourab Panigrahi, Phani Motamarri, David Rogers, Paul Zimmerman, and Vikram Gavini. Large-scale materials modeling at quantum accuracy: Ab initio simulations of quasicrystals and interacting extended defects in metallic alloys. In *Proceedings of the International Conference for High Performance Computing, Networking, Storage and Analysis*, pages 1–12, 2023.

[11] Sambit Das, Phani Motamarri, Vishal Subramanian, David M Rogers, and Vikram Gavini. DFT-FE 1.0: A massively parallel hybrid CPU-GPU density functional theory code using finite-element discretization. *Computer Physics Communications*, 280:108473, 2022.

[12] Antonius Dorda and Ferdinand Schürrer. A WENO-solver combined with adaptive momentum discretization for the Wigner transport equation and its application to resonant tunneling diodes. *Journal of Computational Physics*, 284:95–116, 2015.

[13] William R. Frensley. Wigner-function model of a resonant-tunneling semiconductor device. *Physical Review B*, 36:1570–1580, Jul 1987.

[14] William R. Frensley. Boundary conditions for open quantum systems driven far from equilibrium. *Reviews of Modern Physics*, 62:745–791, Jul 1990.

[15] Oliver Furtmaier, Sauro Succi, and Miller Mendoza. Semi-spectral method for the Wigner equation. *Journal of Computational Physics*, 305:1015–1036, 2016.

[16] Irene Gamba, Maria Pia Gualdani, and Richard W. Sharp. An adaptable discontinuous Galerkin scheme for the Wigner-Fokker-Planck equation. *Communications in Mathematical Sciences*, 7(3):635–664, 2009.

[17] MOSM Hillery, Robert F. O’Connell, Marlan O. Scully, and Eugene P. Wigner. Distribution functions in physics: Fundamentals. *Physics Reports*, 106(3):121–167, 1984.

[18] Pierre Hohenberg and Walter Kohn. Inhomogeneous electron gas. *Physical review*, 136(3B):B864, 1964.

[19] Matthias Hug, Christoph Menke, and Wolfgang P. Schleich. Modified spectral method in phase space: Calculation of the Wigner function. I. Fundamentals. *Physical Review A*, 57:3188–3205, May 1998.

[20] Matthias Hug, Christoph Menke, and Wolfgang P. Schleich. Modified spectral method in phase space: Calculation of the Wigner function. II. Generalizations. *Physical Review A*, 57:3206–3224, May 1998.

[21] A. S. Larkin and V. S. Filinov. Phase space path integral representation for Wigner function. *Journal of Applied Mathematics and Physics*, 5:392–411, 2017.

[22] A. S. Larkin, V. S. Filinov, and V. E. Fortov. Path integral representation of the Wigner function in canonical ensemble. *Contributions to Plasma Physics*, 56(3-4):187–196, 2016.

- [23] Ruo Li, Tiao Lu, Yanli Wang, and Wenqi Yao. Numerical validation for high order hyperbolic moment system of Wigner equation. *Communications in Computational Physics*, 15(3):569–595, 2014.
- [24] Lin Lin, Jianfeng Lu, and Lexing Ying. Numerical methods for Kohn–Sham density functional theory. *Acta Numerica*, 28:405–539, 2019.
- [25] RJ Magyar and Kieron Burke. Density-functional theory in one dimension for contact-interacting fermions. *Physical Review A*, 70(3):032508, 2004.
- [26] Phani Motamarri and Vikram Gavini. Subquadratic-scaling subspace projection method for large-scale Kohn-Sham density functional theory calculations using spectral finite-element discretization. *Physical Review B*, 90(11):115127, 2014.
- [27] Ayako Nakata, Jack S. Baker, Shereif Y. Mujahed, Jack T.L. Poulton, Sergiu Arapan, Jianbo Lin, Zamaan Raza, Sushma Yadav, Lionel Truflandier, Tsuyoshi Miyazaki, et al. Large scale and linear scaling DFT with the CONQUEST code. *Journal of Chemical Physics*, 152(16), 2020.
- [28] Mihail Nedjalkov, Hans Kosina, Siegfried Selberherr, Christian Ringhofer, and David K. Ferry. Unified particle approach to Wigner-Boltzmann transport in small semiconductor devices. *Physical Review B*, 70:115319, Sep 2004.
- [29] Mihail Nedjalkov, Philipp Schwaha, Siegfried Selberherr, Jean Michel Sellier, and Dragica Vasileska. Wigner quasi-particle attributes—an asymptotic perspective. *Applied Physics Letters*, 102(16):163113, 2013.
- [30] Robert G Parr and Weitao Yang. Density-functional theory of the electronic structure of molecules. *Annual Review of Physical Chemistry*, 46(1):701–728, 1995.
- [31] Yousef Saad, James R. Chelikowsky, and Suzanne M. Shontz. Numerical methods for electronic structure calculations of materials. *SIAM Review*, 52(1):3–54, 2010.
- [32] Philipp Schwaha, Damien Querlioz, Philippe Dollfus, Jérôme Saint-Martin, Mihail Nedjalkov, and Siegfried Selberherr. Decoherence effects in the Wigner function formalism. *Journal of Computational Electronics*, 12:388–396, 2013.
- [33] Jean Michel Sellier and Ivan Dimov. The many-body Wigner Monte Carlo method for time-dependent ab-initio quantum simulations. *Journal of Computational Physics*, 273:589 – 597, 2014.
- [34] Jean Michel Sellier and Ivan Dimov. A Wigner Monte Carlo approach to density functional theory. *Journal of Computational Physics*, 270:265 – 277, 2014.
- [35] Jean Michel Sellier and Ivan Dimov. On the simulation of indistinguishable fermions in the many-body Wigner formalism. *Journal of Computational Physics*, 280:287 – 294, 2015.
- [36] Jean Michel Sellier and Ivan Dimov. On a full Monte Carlo approach to quantum mechanics. *Physica A: Statistical Mechanics and its Applications*, 463:45 – 62, 2016.
- [37] Jean Michel Sellier, Mihail Nedjalkov, and Ivan Dimov. An introduction to applied quantum mechanics in the Wigner Monte Carlo formalism. *Physics Reports*, 577:1–34, 2015.
- [38] Jean Michel Sellier, Mihail Nedjalkov, Ivan Dimov, and Siegfried Selberherr. A benchmark study of the Wigner Monte Carlo method. *Monte Carlo Methods and Applications*, 20(1):43 – 51, 01 Mar. 2014.
- [39] Lu Jeu Sham and Walter Kohn. One-particle properties of an inhomogeneous interacting electron gas. *Physical Review*, 145(2):561, 1966.

[40] Sihong Shao, Tiao Lu, and Wei Cai. Adaptive conservative cell average spectral element methods for transient Wigner equation in quantum transport. *Communications in Computational Physics*, 9(3):711–739, 2011.

[41] Sihong Shao and Yunfeng Xiong. Branching random walk solutions to the Wigner equation. *SIAM Journal on Numerical Analysis*, 58(5):2589–2608, 2020.

[42] Michael Springborg and Jens Peder Dahl. Wigner’s phase-space function and atomic structure II. Ground states for closed-shell atoms. *Physical Review A*, 36:1050–1062, Aug 1987.

[43] Gilbert Strang. On the construction and comparison of difference schemes. *SIAM Journal on Numerical Analysis*, 5(3):506–517, 1968.

[44] Bassano Vacchini and Klaus Hornberger. Relaxation dynamics of a quantum Brownian particle in an ideal gas. *The European Physical Journal Special Topics*, 151(1):59–72, 2007.

[45] Maarten L Van de Put, Bart Sorée, and Wim Magnus. Efficient solution of the Wigner–Liouville equation using a spectral decomposition of the force field. *Journal of Computational Physics*, 350:314–325, 2017.

[46] Josef Weinbub and D. K. Ferry. Recent advances in Wigner function approaches. *Applied Physics Reviews*, 5(4):041104, 2018.

[47] Eugene P. Wigner. On the quantum correction for thermodynamic equilibrium. *Physical Review*, 40:749–759, 1932.

[48] Yunfeng Xiong, Zhenzhu Chen, and Sihong Shao. An advective-spectral-mixed method for time-dependent many-body Wigner simulations. *SIAM Journal on Scientific Computing*, 38(4):B491–B520, 2016.

[49] Yunfeng Xiong, Yong Zhang, and Sihong Shao. A characteristic-spectral-mixed scheme for six-dimensional Wigner–Coulomb dynamics. *SIAM Journal on Scientific Computing*, 45(6):B906–B931, 2023.

[50] Dongsheng Yin, Min Tang, and Shi Jin. The Gaussian beam method for the Wigner equation with discontinuous potentials. *Inverse Problems & Imaging*, 7(1930-8337, 2013, 3, 1051):1051, 2013.

[51] Cosmas K. Zachos. Deformation quantization: Quantum mechanics lives and works in phase-space. *International Journal of Modern Physics A*, 17(03):297–316, 2002.

[52] Hongfei Zhan, Zhenning Cai, and Guanghui Hu. The Wigner function of ground state and one-dimensional numerics. *Journal of Computational Physics*, 449:110780, 2022.

[53] Zhimin Zhang. How many numerical eigenvalues can we trust? *Journal of Scientific Computing*, 65(2):455–466, 2015.